

# Limits on Second-Order Non-Gaussianity from Minkowski Functionals of WMAP Data

Chiaki Hikage<sup>1\*</sup>, Takahiko Matsubara<sup>1,2</sup>

<sup>1</sup> *Kobayashi-Maskawa Institute, Nagoya University, Nagoya 464-8602, Japan*

<sup>2</sup> *Department of Physics, Nagoya University, Nagoya 464-8602, Japan*

14 August 2018

## ABSTRACT

We analyze non-Gaussianity (NG) due to the primordial bispectrum and trispectrum using cosmic microwave background temperature maps of WMAP 7-year data. We first apply the perturbative formulae of Minkowski functionals (MFs) up to second-order NG derived by Matsubara (2010), which enable us to give limits on cubic NG parametrized with  $\tau_{\text{NL}}$  and  $g_{\text{NL}}$  as well as various types of quadratic NG parametrized with  $f_{\text{NL}}$ . We find no signature of primordial NG in WMAP 7-year data, but give constraints on the local-type, equilateral-type, orthogonal-type  $f_{\text{NL}}$ :  $f_{\text{NL}}^{(\text{loc})} = 20 \pm 42$ ,  $f_{\text{NL}}^{(\text{eq})} = -121 \pm 208$ , and  $f_{\text{NL}}^{(\text{ort})} = -129 \pm 171$ , respectively, and  $\tau_{\text{NL}}/10^4 = -7.6 \pm 8.7$ , and  $g_{\text{NL}}/10^5 = -1.9 \pm 6.4$ . We also find that these constraints are consistent with the limits from skewness and kurtosis parameters which characterize the perturbative corrections of MFs.

**Key words:** Cosmology: early Universe – cosmic microwave background – methods: statistical – analytical

## 1 INTRODUCTION

Non-Gaussianity (NG) in primordial curvature perturbation is a key observational probe to study physics in early Universe. Single slowly-rolling scalar inflation model predicts too small NG to be observed (Salopek & Bond 1990; Falk et al. 1993; Gangui et al. 1994; Acquaviva et al. 2003; Maldacena 2003; Bartolo, Matarrese & Riotto 2006). Variants of the simple inflationary models generate much higher levels of NG: multiple fields (Linde & Mukhanov 1997; Lyth, Ungarelli & Wands 2003); modulated reheating scenarios (Dvali, Gruzinov & Zaldarriaga 2004); warm inflation (Gupta et al. 2002; Moss & Xiong 2007); ekpyrotic model (Koyama et al. 2007; Creminelli, & Senatore 2007; Buchbinder, Khoury & Ovrut 2007). These NGs have been constrained using the cubic-order statistics (i.e., bispectrum) from CMB temperature maps of WMAP (Komatsu et al. 2011; Creminelli, Senatore, & Zaldarriaga 2007; Yadav & Wandelt 2008; Curto et al. 2011).

So far NG analysis has been mainly focused on the measurement of primordial bispectrum. Primordial trispectrum, the next higher-order term, also provides an important probe to differentiate inflation models. Trispectrum is generally described into two different kinds of connected parts and their amplitudes is commonly parametrized by  $g_{\text{NL}}$  and  $\tau_{\text{NL}}$  (e.g.,

Okamoto & Hu 2002). So-called local-type NG is described as the nonlinear correction in Bardeen’s curvature as follows:

$$\Phi = \phi + f_{\text{NL}}(\phi^2 - \langle \phi^2 \rangle) + g_{\text{NL}}\phi^3 \dots, \quad (1)$$

(e.g., Kogo & Komatsu 2006) where  $\phi$  is an auxiliary Gaussian variable and  $\Phi$  is related to the curvature perturbation  $\zeta$  as  $\Phi = 3/5\zeta$ . In this local-type model,  $\tau_{\text{NL}}$  is equal to  $36f_{\text{NL}}^2/25$ . Suyama & Yamaguchi (2008) find that all classes of multi-inflation models satisfy the inequality condition  $\tau_{\text{NL}} \geq 36f_{\text{NL}}^2/25$  derived from the Cauchy-Schwarz inequality. The relation between  $\tau_{\text{NL}}$  and  $f_{\text{NL}}$  is therefore another powerful probe of inflation models (e.g., Suyama et al. 2010). Current WMAP constraints on  $\tau_{\text{NL}}$  and  $g_{\text{NL}}$  are obtained by several groups:  $-5.6 < g_{\text{NL}}/10^5 < 6.4$  (95%C.L.) from the N-point probability density function (Vielva & Sanz 2010);  $-12.4 < g_{\text{NL}}/10^5 < 15.6$  (95%C.L.) using trispectrum (Fergusson, Regan, Shellard 2010);  $-0.6 < \tau_{\text{NL}}/10^4 < 3.3$  (95%C.L.) and  $-7.4 < g_{\text{NL}}/10^5 < 8.2$  (95%C.L.) using kurtosis power spectrum (Smidt et al. 2010). Planck is expected to reach  $\Delta\tau_{\text{NL}} \sim 560$  (Kogo & Komatsu 2006).

Full analysis of trispectrum is computationally very expensive because their number of configurations are enormous. Minkowski functionals (MFs) are another powerful tool to constrain NGs from the aspect of morphological properties of the density structure. MFs and polyspectrum such as bispectrum and trispectrum are very different statistics. MFs are real-space statistics, whereas the polyspectrum is defined in harmonic space. MFs naturally incorporate the information of all orders

\* hikage@kmi.nagoya-u.ac.jp

of polyspectra and thus they are complementary to the commonly used measurement using polyspectra. According to the perturbative formulae of MFs derived by Matsubara (2010), the higher-order NG originated from primordial trispectrum is characterized with four kurtosis parameters, which is the summation over trispectrum with different weights on tetrahedron configuration. The computation of kurtosis parameters is much less expensive compared to the trispectrum estimator. MFs are model-independent statistics and hence they have a potential to serendipitously find NGs due to unknown sources that has not been explored. Consistency check using different estimators from the standard one is thereby important to obtain more robust results.

In this paper, we first apply the perturbative formulae of MFs upto 2nd-order derived by Matsubara (2010) to WMAP 7-year data of CMB temperature anisotropies. We give new constraints on  $\tau_{\text{NL}}$  and  $g_{\text{NL}}$  as well as local, equilateral, and orthogonal types of  $f_{\text{NL}}$ s. This paper is the extension of the previous work to give limits on the local-type  $f_{\text{NL}}$  from MFs of WMAP 3-year data Hikage et al. (2008) and BOOMERanG data Natoli et al. (2010).

The paper is organized as follows: in section 2, we review the perturbative formulae derived by Matsubara (2010). In section 3, we compare the perturbative predictions with numerical simulations. We apply the perturbative formulae to the WMAP data and constrain different NG parameters in section 4. Section 5 is devoted to the summary and discussions.

## 2 PERTURBATIVE FORMULAE OF MINKOWSKI FUNCTIONALS FOR CMB TEMPERATURE MAPS WITH PRIMORDIAL NG

### 2.1 Minkowski Functionals for Gaussian Fields

Minkowski functionals (MFs) have been used to characterize the morphology of a given density field (Mecke et al. 1994; Schmalzing & Buchert 1997). In 2-dimensional field such as CMB temperature maps, three MFs are defined: area fraction ( $V_0$ ), circumference ( $V_1$ ), and Euler characteristics ( $V_2$ ). We measure them for the area whose temperature anisotropy  $f \equiv \Delta T/T$  normalized by the standard deviation  $\sigma_0 \equiv \langle f^2 \rangle^{1/2}$  is larger than a threshold value  $\nu$ . In Gaussian temperature maps, the  $k$ -th MF  $V_k^{(\text{G})}$  is given by

$$V_k^{(\text{G})}(\nu) = A_k \exp\left(-\frac{\nu^2}{2}\right) H_{k-1}(\nu), \quad (2)$$

where  $H_k(\nu)$  represent the  $k$ -th Hermite polynomials. The amplitude  $A_k$  is given by

$$A_k = \frac{1}{(2\pi)^{(k+1)/2}} \frac{\omega_2}{\omega_{2-k}\omega_k} \left(\frac{\sigma_1}{\sqrt{2}\sigma_0}\right)^k, \quad (3)$$

where  $\omega_k \equiv \pi^{k/2}/\Gamma(k/2 + 1)$ . The standard deviation  $\sigma_0$  and that of the first derivative  $\sigma_1 \equiv \langle |\nabla f|^2 \rangle^{1/2}$  are written as a sum of the power spectrum  $C_l$ :

$$\sigma_j^2 \equiv \frac{1}{4\pi} \sum_l (2l+1) [l(l+1)]^j C_l W_l^2, \quad (4)$$

where  $W_l$  represents the smoothing kernel determined by the pixel and beam window functions and any additional smoothing. Here we use Gaussian kernel  $W_l = \exp(-l(l+1)\theta^2/2)$  and

$\theta$  denotes the smoothing angular scale. Table 1 lists HEALPix pixel number  $N_{\text{side}}$  (the total pixel number is  $12N_{\text{side}}^2$ ) and the maximum multipole number  $l_{\text{max}}$  at different values of  $\theta$ . We choose the values of  $N_{\text{side}}$  and  $l_{\text{max}}$  so that the effects of pixel window and high frequency cut be small. As discussed later, measuring MFs of CMB maps with different smoothing scales is important to extract configuration dependence contained in primordial bispectrum and trispectrum.

### 2.2 Perturbative Formulae in Weakly Non-Gaussian Fields

Matsubara (2003) has applied multivariate Edgeworth expansion theorem to derive perturbative formulae of MFs for a general field. Matsubara (2010) extended his analysis and derived 2nd-order correction of MFs on CMB temperature maps. According to their works, the MFs of a weakly NG field (i.e.  $\sigma_0 \ll 1$ ) are written upto the 2nd-order term of  $\sigma_0$  as

$$V_k(\nu) = V_k^{(\text{G})}(\nu) + A_k e^{-\nu^2/2} \Delta v_k(\nu), \quad (5)$$

$$\Delta v_k(\nu) = v_k^{(1)}(\nu)\sigma_0 + v_k^{(2)}(\nu)\sigma_0^2. \quad (6)$$

In the following subsection, we review the perturbative formulae for a CMB temperature map.

#### 2.2.1 First-order perturbation

The 1st-order perturbation terms of MFs are characterized by three skewness parameters:

$$v_k^{(1)}(\nu) = \frac{S}{6} H_{k+2}(\nu) - \frac{S_{\text{I}}}{2} H_k(\nu) - \frac{S_{\text{II}}}{2} H_{k-2}(\nu), \quad (7)$$

with

$$S \equiv \frac{\langle f^3 \rangle}{\sigma_0^3}, \quad S_{\text{I}} \equiv \frac{f^2 \langle \nabla^2 f \rangle}{\sigma_0^2 \sigma_1^2}, \quad S_{\text{II}} \equiv \frac{2 \langle |\nabla f|^2 \nabla^2 f \rangle}{\sigma_1^4}. \quad (8)$$

The skewness parameters are written as the sum of the bispectrum with different weights of triangle configurations:

$$S_A = \frac{1}{4\pi\sigma_0^4} \sum_{l_1, l_2, l_3} I_{l_1 l_2 l_3} \tilde{S}_{A l_1 l_2 l_3} B_{l_1 l_2 l_3} W_{l_1} W_{l_2} W_{l_3}, \quad (9)$$

where

$$\tilde{S}_{l_1 l_2 l_3} = 1, \quad (10)$$

$$\tilde{S}_{\text{I} l_1 l_2 l_3} = -\frac{\{l_1\} + \{l_2\} + \{l_3\}}{6q^2}, \quad (11)$$

$$\tilde{S}_{\text{II} l_1 l_2 l_3} = \frac{1}{12q^4} [\{l_1\}^2 + \{l_2\}^2 + \{l_3\}^2 - 2(\{l_1\}\{l_2\} + \{l_2\}\{l_3\} + \{l_3\}\{l_1\})], \quad (12)$$

with  $q = \sigma_1/\sqrt{2}\sigma_0$  and  $\{l\} \equiv l(l+1)$ , and

$$I_{l_1 l_2 l_3} \equiv \sqrt{\frac{(2l_1+1)(2l_2+1)(2l_3+1)}{4\pi}} \begin{pmatrix} l_1 & l_2 & l_3 \\ 0 & 0 & 0 \end{pmatrix}. \quad (13)$$

Note that the proportional factor of the skewness parameters are different from the parameters  $S^{(i)}$  used in Matsubara (2003); Hikage, Komatsu & Matsubara (2006) and their relations are  $S = S^{(0)}$ ,  $S_{\text{I}} = -4S^{(1)}/3$  and  $S_{\text{II}} = -2S^{(2)}/3$ . The three skewness parameters have different weights of the bispectrum and hence the MFs can extract more information on the configuration dependence of bispectrum than using only one skewness value of  $S$ . The bispectrum  $B_{l_1 l_2 l_3}$  is defined as

$$\langle a_{l_1 m_1} a_{l_2 m_2} a_{l_3 m_3} \rangle_c \equiv \begin{pmatrix} l_1 & l_2 & l_3 \\ m_1 & m_2 & m_3 \end{pmatrix} B_{l_1 l_2 l_3}. \quad (14)$$

where  $a_{lm}$  is the harmonic coefficients of a given temperature anisotropy map. The relation to the reduce bispectrum  $b_{l_1 l_2 l_3}$  is  $B_{l_1 l_2 l_3} = I_{l_1 l_2 l_3} b_{l_1 l_2 l_3}$ . We consider three different types of NGs due to primordial bispectra: local type, equilateral type, and orthogonal type. Single and multi-field inflation models predict local-type NG (eq.[1]), which generates the following form of CMB bispectrum (e.g., Komatsu & Spergel 2001):

$$B_{l_1 l_2 l_3} = 2f_{\text{NL}}^{(\text{loc})} I_{l_1 l_2 l_3} \int r^2 dr [\alpha_{l_1}(r)\beta_{l_2}(r)\beta_{l_3}(r) + \text{cyclic}], \quad (15)$$

with

$$\alpha_l(r) \equiv \frac{2}{\pi} \int k^2 dk g_{Tl}(k) j_l(kr), \quad (16)$$

$$\beta_l(r) \equiv \frac{2}{\pi} \int k^2 dk P_\phi(k) g_{Tl}(k) j_l(kr), \quad (17)$$

where  $g_{Tl}$  is the radiation transfer function and  $j_l$  is the spherical Bessel function. We rewrite  $f_{\text{NL}}$  as  $f_{\text{NL}}^{(\text{loc})}$ . The local-type NG is sensitive to the bispectrum with squeezed configuration of triangle wavevectors ( $l_1 \ll l_2 \simeq l_3$ ).

Other inflation scenarios with non-canonical kinetic terms (Seery & Lidsey 2005; Chen, Easther & Lim 2007), Dirac-Born-Infeld models (Alishahiha et al. 2004), and Ghost inflation (Arkani-Hamed et al. 2004) predict large NG signals in equilateral configuration triangles ( $l_1 \simeq l_2 \simeq l_3$ ). Equilateral-type NG is characterized with  $f_{\text{NL}}^{(\text{eq})}$  defined as the amplitude of the following bispectrum (Babich, Creminelli & Zaldarriaga 2004):

$$B_{l_1 l_2 l_3}^{(\text{eq})} = 6f_{\text{NL}}^{(\text{eq})} I_{l_1 l_2 l_3} \int r^2 dr [-\beta_{l_1}(r)\beta_{l_2}(r)\alpha_{l_3}(r) - \beta_{l_1}(r)\alpha_{l_2}(r)\beta_{l_3}(r) - \alpha_{l_1}(r)\beta_{l_2}(r)\beta_{l_3}(r) - 2\delta_{l_1}(r)\delta_{l_2}(r)\delta_{l_3}(r) + \{\beta_{l_1}(r)\gamma_{l_2}(r)\delta_{l_3}(r) + (5\text{permutation})\}], \quad (18)$$

where

$$\gamma_l(r) \equiv \frac{2}{\pi} \int k^2 dk P_\phi^{1/3}(k) g_{Tl}(k) j_l(kr), \quad (19)$$

$$\delta_l(r) \equiv \frac{2}{\pi} \int k^2 dk P_\phi^{2/3}(k) g_{Tl}(k) j_l(kr). \quad (20)$$

The other type of NG which is sensitive to the bispectrum with a folded triangle configuration ( $l_1 \simeq l_2 \simeq l_3/2$ ) is also considered by Senatore, Tassev, Zaldarriaga (2009). This is called orthogonal-type NG and characterized by  $f_{\text{NL}}^{(\text{ort})}$ :

$$B_{l_1 l_2 l_3}^{(\text{ort})} = 6f_{\text{NL}}^{(\text{ort})} I_{l_1 l_2 l_3} \int r^2 dr [-3\beta_{l_1}(r)\beta_{l_2}(r)\alpha_{l_3}(r) - 3\beta_{l_1}(r)\alpha_{l_2}(r)\beta_{l_3}(r) - 3\alpha_{l_1}(r)\beta_{l_2}(r)\beta_{l_3}(r) - 8\delta_{l_1}(r)\delta_{l_2}(r)\delta_{l_3}(r) + 3\{\beta_{l_1}(r)\gamma_{l_2}(r)\delta_{l_3}(r) + (5\text{perm.})\}]. \quad (21)$$

As discussed in Sec. 4.2 of Senatore, Tassev, Zaldarriaga (2009), we include the integration of  $r$  further than the last scattering surface  $r_*$  to calculate the equilateral and orthogonal-type bispectra. This reduces the sensitivity of these types of NG.

We also take into account the effect of unmasked point sources (e.g., radio galaxies) which generates an additional NG in observed CMB maps. Assuming them to be Poisson distribution, the bispectrum has a constant value for all configurations of wavevectors:

$$B_{l_1 l_2 l_3}^{(\text{ps})} = b^{(\text{ps})} I_{l_1 l_2 l_3}. \quad (22)$$

where  $b^{(\text{ps})}$  is a constant value.

Fig. 1 plots the smoothing scale dependence of three skewness parameters (eq.[8]) from the local-type, equilateral-type, orthogonal-type primordial NG components with the unity value of  $f_{\text{NL}}$  and from unmasked point source NG with the constant bispectrum  $b^{(\text{ps})} = 10^{-27}$ . We add noise and beam functions of WMAP 7-year V+W co-added maps which become important at smaller smoothing scale such as  $\theta < 10$  arcmin. Scale dependences of skewness parameters are quite different among different NG types. Measuring MFs of CMB maps with different smoothing scales is important to break degeneracy of different NG sources.

## 2.2.2 Second-order perturbation

Matsubara (2010) has derived the second-order corrections of MFs, which are characterized with the product of skewness parameters and four kurtosis parameters:

$$v_0^{(2)}(\nu) = \frac{S^2}{72} H_5(\nu) + \frac{K}{24} H_3(\nu), \quad (23)$$

$$v_1^{(2)}(\nu) = \frac{S^2}{72} H_6(\nu) + \frac{K - SS_{\text{I}}}{24} H_4(\nu) - \frac{1}{12} \left( K_{\text{I}} + \frac{3}{8} S_{\text{I}}^2 \right) H_2(\nu) - \frac{K_{\text{III}}}{8}, \quad (24)$$

$$v_2^{(2)}(\nu) = \frac{S^2}{72} H_7(\nu) + \frac{K - 2SS_{\text{I}}}{24} H_5(\nu) - \frac{1}{6} \left( K_{\text{I}} + \frac{1}{2} SS_{\text{II}} \right) H_3(\nu) - \frac{1}{2} \left( K_{\text{II}} + \frac{1}{2} S_{\text{I}} S_{\text{II}} \right) H_1(\nu). \quad (25)$$

The kurtosis parameters are defined as

$$K \equiv \frac{\langle f^4 \rangle_c}{\sigma_0^4}, \quad K_{\text{I}} \equiv \frac{\langle (\nabla^2 f) f^3 \rangle_c}{\sigma_0^4 \sigma_1^2}, \quad (26)$$

$$K_{\text{II}} \equiv \frac{2\langle f |\nabla f|^2 \nabla^2 f \rangle_c + \langle |\nabla f|^4 \rangle_c}{\sigma_0^2 \sigma_1^4}, \quad K_{\text{III}} \equiv \frac{\langle |\nabla f|^4 \rangle_c}{2\sigma_0^2 \sigma_1^4}, \quad (27)$$

where  $\langle \dots \rangle_c$  denotes the ensemble average of the connected part.

For the local-type NG, the reduced trispectrum is written as

$$\mathcal{T}_{l_3 l_4}^{l_1 l_2}(L) = I_{l_1 l_2 L} I_{l_3 l_4 L} \left\{ \frac{25}{9} \tau_{\text{NL}} \int r_1^2 dr_1 r_2^2 dr_2 F_L(r_1, r_2) \times \alpha_{l_1}(r_1) \beta_{l_2}(r_1) \alpha_{l_3}(r_2) \beta_{l_4}(r_2) + g_{\text{NL}} \int r^2 dr \beta_{l_2}(r) \beta_{l_4}(r) [\alpha_{l_1}(r) \beta_{l_3}(r) + \beta_{l_1}(r) \alpha_{l_3}(r)] \right\}, \quad (28)$$

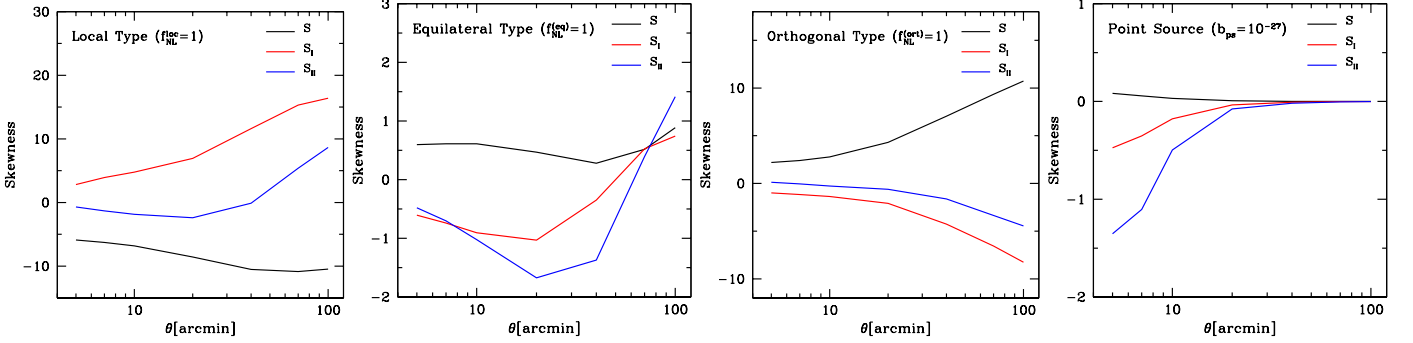
where

$$F_L(r_1, r_2) \equiv \frac{2}{\pi} \int k^2 dk P_\phi(k) j_L(kr_1) j_L(kr_2). \quad (29)$$

For the single-field inflation model with local-type NG (eq.[1]),  $\tau_{\text{NL}}$  is equal to  $36f_{\text{NL}}^{(\text{loc})2}/25$ .

The kurtosis parameters are given by a summation over all configurations of trispectra. The full calculation of trispectra is, however, computationally very expensive and hence we estimate kurtosis values using Monte-Carlo integration of the flat-sky approximation. Matsubara (2010) finds that the full-sky spectrum with its multipole configuration of  $\{l_i\}$  is well approximated by the flat-sky spectrum with the wavelength

**Figure 1.** Three Skewness values (eq.[8]) for local-type (eq.[15]), equilateral-type (eq.[18]), and orthogonal-type (eq.[21]) NGs and point sources as a function of the Gaussian smoothing scale  $\theta$ . We add WMAP beam functions for V+W co-added maps and a pixel window function corresponding to each  $\theta$  listed in Table 1.



configuration of  $l_i + 1/2$ :

$$\mathcal{T}_{l_3 l_4}^{l_1 l_2}(L) \simeq I_{l_1 l_2 L} I_{l_3 l_4 L} \times \mathcal{T} \left( l_1 + \frac{1}{2}, l_2 + \frac{1}{2}, l_3 + \frac{1}{2}, l_4 + \frac{1}{2}; L + \frac{1}{2} \right). \quad (30)$$

The proportional factor  $I_{l_1 l_2 L} I_{l_3 l_4 L}$  has non-zero value when both  $l_1 + l_2 + L$  and  $l_3 + l_4 + L$  have even number. Note that the difference of  $1/2$  for all arguments of lengths  $l$  is very important for the accurate estimation. The kurtosis in flat-sky approximation is given as

$$K_A = \frac{1}{\sigma_0^6} \int \frac{l_1 dl_1}{2\pi} \frac{l_2 dl_2}{2\pi} \frac{l_3 dl_3}{2\pi} \frac{d\theta_{12}}{2\pi} \frac{d\theta_{23}}{2\pi} \tilde{K}_A(l_1, l_3, l_{12}) \times T(l_1, l_2, l_3, l_4; l_{12}, l_{23}) W(l_1) W(l_2) W(l_3) W(l_4), \quad (31)$$

where

$$\tilde{K} = 1, \quad \tilde{K}_I = -\frac{l_1^2}{2q^2}, \quad \tilde{K}_{II} = -\frac{l_{12}^2 - 4l_1^2 l_3^2}{16q^4}, \quad \tilde{K}_{III} = \frac{l_{12}^4 + 4l_1^2 (l_3^2 - l_{12}^2)}{32q^4}, \quad (32)$$

and the Gaussian window function in the flat approximation is now given by  $W(l) = \exp[-\{(l + 1/2)\theta\}^2/2]$ . The trispectrum  $T$  is symmetric against the arbitrary exchange of arguments among  $l_1, l_2, l_3$  and  $l_4$  and then it is given as a sum of the reduced trispectrum  $\mathcal{T}$ :

$$T(l_1, l_2, l_3, l_4; l_{12}, l_{23}) = P(l_1, l_2, l_3, l_4, l_{12}) + P(l_1, l_3, l_2, l_4, l_{13}) + P(l_1, l_4, l_2, l_3, l_{23}), \quad (33)$$

and

$$P(l_1, l_2, l_3, l_4, L) = \mathcal{T}(l_1, l_2, l_3, l_4, L) + \mathcal{T}(l_2, l_1, l_3, l_4, L) + \mathcal{T}(l_1, l_2, l_4, l_3, L) + \mathcal{T}(l_2, l_1, l_4, l_3, L). \quad (34)$$

As shown in Fig. 2, the quadrangle configuration is uniquely determined by five parameter spaces: three side lengths  $l_1, l_2, l_3$  and their open angles  $\theta_{12}, \theta_{23}$ . The other side length  $l_4$ , two diagonal lengths  $l_{12}$  and  $l_{23}$  (see Fig. 2) and  $l_{13} = |\mathbf{l}_1 + \mathbf{l}_3|$  are written in terms of the five parameters. Fortunately, the configuration dependence of the trispectrum is smooth for the local-type NG model and hence Monte Carlo integration is applicable to estimate kurtosis values in shorter time. The integration of the side lengths  $l_1, l_2$  and  $l_3$  is done from 2 to  $l_{\max}$  given by Table 1 and that of  $\theta_{12}$  and  $\theta_{23}$  is done from 0 to  $2\pi$ . In equation (30), the fractional values of the length  $\{l_i\}$  are allowed in the flat-sky approximation of  $\mathcal{T}$ , while the full-sky

**Figure 2.** Trispectrum of two-dimensional CMB maps is calculated at each configuration of tetrahedron. A tetrahedron is uniquely determined by three side lengths  $l_1, l_2, l_3$  and their open angles  $\theta_{12}$  and  $\theta_{23}$ . The other side length  $l_4$  and the diagonal lines  $l_{12}$  and  $l_{23}$  used in the equation (33) are also shown.

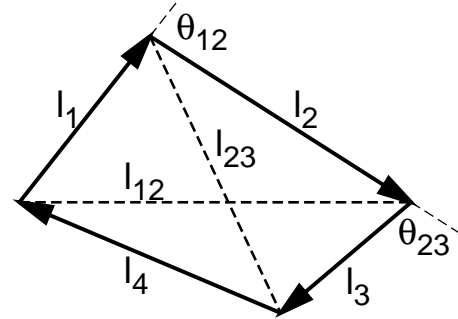


**Table 1.** Resolution scale  $N_{\text{side}}$  for HEALPix (total number of pixels is given by  $12N_{\text{side}}^2$ ) and the maximum values of multipole  $l_{\max}$  at each smoothing scale  $\theta$  [arcmin].

$\theta$ [arcmin]	$N_{\text{side}}$	$l_{\max}$
100	128	136
70	128	196
40	256	340
20	512	684
10	512	750
7	512	1024
5	512	1250

trispectrum  $\mathcal{T}_{l_3 l_4}^{l_1 l_2}(L)$  is only given for a set of integer values  $l_i$ . We use the round-off values of  $\{l_i\}$  to get  $\mathcal{T}$ . We get the reasonable values of kurtosis parameters by  $\mathcal{O}(10^9)$  calculation, which takes much shorter time than the full calculation of the trispectrum.

For the trispectrum, we also consider the effect of point source as

$$\mathcal{T}_{l_3 l_4}^{l_1 l_2}(L) = t^{(\text{ps})} I_{l_1 l_2 L} I_{l_3 l_4 L}, \quad (35)$$

where  $t^{(\text{ps})}$  is a constant value.



### 3 COMPARISON OF PERTURBATION THEORY WITH NUMERICAL SIMULATIONS

#### 3.1 Computation of Minkowski Functionals from CMB maps

Computation method of the MFs of CMB maps are described in Appendix A.1. of Hikage, Komatsu & Matsubara (2006). The range of  $\nu$  is from  $-3.6$  to  $3.6$  and the binning number is set to be 36 for each MF with the equal binning width  $\Delta\nu = 0.2$ . The numerical estimations of 2nd and 3rd MFs do not completely agree with the analytical predictions even in Gaussian fields. Lim & Simon (2012) found that the deviation comes from the approximation of the delta function with a finite difference. In Gaussian fields, the correction terms of the finite binning effect of the 2nd and 3rd MFs are given by

$$\begin{aligned} R_k(\nu) &\equiv \left[ \frac{1}{\Delta\nu} \int_{\nu-\Delta\nu/2}^{\nu+\Delta\nu/2} dx V_k(x) \right] - V_k^{(G)}(\nu) \\ &= \frac{(\Delta\nu)^2}{24} H_{k+1}(\nu) A_k e^{-\nu^2/2} + \mathcal{O}(\Delta\nu^4), \end{aligned} \quad (36)$$

where  $\Delta\nu$  is the binning width of  $\nu$ . We subtract the correction terms from the measured MFs.

#### 3.2 Comparison of Perturbation Theory with Non-Gaussian CMB Maps

Actual CMB maps have various observational effects such as survey geometry, inhomogeneous noise, which may cause systematic uncertainty in the NG measurements from MFs. We take into account such observational systematics by constructing realistic CMB simulation maps and test if the perturbation works for actual observations.

##### 3.2.1 Full Non-Gaussian Simulations

We employ 1000 realizations of simulated CMB maps with a local-type NG available in public (Elsner & Wandelt 2009). These simulation maps include full radiation transfer function. We make mock CMB maps as described in Hikage et al. (2008): making Gaussian CMB maps with their input power spectra following WMAP 7-year cosmology and including the beam function for each differencing assembly (DA), we add Gaussian-distributed noise to each pixel with the standard deviation of  $\sigma/N_{\text{obs}}$  in WMAP 7-year observations. We co-add noise-included DA maps with the inverse weight of averaged noise variance and then mask the area outside the KQ75 mask of Galactic foregrounds and point sources (Gold et al. 2011).

Fig. 3 (left-hand panels) shows a comparison of two variances (eq.[4]), three skewness parameters (eq.[8]), and four kurtosis parameters (eq.[26]) with  $f_{\text{NL}}^{(\text{loc})} = 300$  between analytical estimations and simulation results at different values of  $\theta_s$ . The simulations do not include the  $g_{\text{NL}}$  term and thereby the second-order NG comes from the square of the  $f_{\text{NL}}$  term, or  $\tau_{\text{NL}}$ . The error-bars represent the  $1\sigma$  dispersion of simulation results divided by the square root of 1000, that is, the number of realizations. The right-hand panels show that the 2nd-order correction of each MF at  $\theta = 10$  arcmin. In the plot of MFs, we subtract Gaussian and 1st-order perturbative correction to focus on the 2nd-order correction (Hikage et al. (2008) have already shown that the 1st-order perturbative correction of MFs due to  $f_{\text{NL}}^{(\text{loc})}$  agree with the results from NG simulations). We

find that the 2nd-order perturbative corrections of MFs also agree with simulation results very well even including the observational effects.

##### 3.2.2 Sachs-Wolfe approximations

We also compare the 2nd-order correction due to  $g_{\text{NL}}$  type using NG simulation maps in Sachs-Wolfe approximation where the NG is locally given by

$$\frac{\Delta T_{\text{SW}}}{T} = \frac{\Delta T_{\text{G}}}{T} - 3f_{\text{NL}}^{(\text{loc})} \left( \frac{\Delta T_{\text{G}}}{T} \right)^2 + 9g_{\text{NL}} \left( \frac{\Delta T_{\text{G}}}{T} \right)^3. \quad (37)$$

The angular power spectrum is set to be  $l(l+1)C_l^{\text{SW}}/2\pi = 10^{-10}$  at  $l \leq l_{\text{max}}$  where  $l_{\text{max}}$  is given in Table 1 at each  $\theta$ . We generate 6000 realizations with  $f_{\text{NL}}^{(\text{loc})} = 100$  and  $g_{\text{NL}} = 10^6$ . For these values, the 1st-order correction from  $f_{\text{NL}}^{(\text{loc})}$  and the 2nd-order correction from  $g_{\text{NL}}$  have comparable amplitudes, but the contribution of  $\tau_{\text{NL}} \sim f_{\text{NL}}^{(\text{loc})2}$  is negligible. Fig. 4 shows a similar plot to that of Fig. 3 but for the comparison with simulations in the Sachs-Wolfe approximation. The right-hand panel shows the MFs subtracting only Gaussian terms at  $\theta = 10$  arcmin. Matsubara (2010) showed that the perturbation formulae work very well in the Sachs-Wolfe approximation. Here we find that the perturbation also works even including the various observational effects such as survey mask, inhomogeneous noise and beam window function. The excellent agreement indicates that the flat-sky approximation and Monte Carlo integration also work very well at a wide range of scales.

#### 3.3 Distribution of NG parameters estimated from simulations

We estimate the bestfit values and the errors of each NG parameter by the least chi-square fitting of observed MFs with the perturbative predictions:

$$\chi^2 = \sum_{i,j} [V_i^{(\text{obs})} - V_i^{(\text{theory})}(p_k)] C_{ij}^{-1} [V_j^{(\text{obs})} - V_j^{(\text{theory})}(p_k)], \quad (38)$$

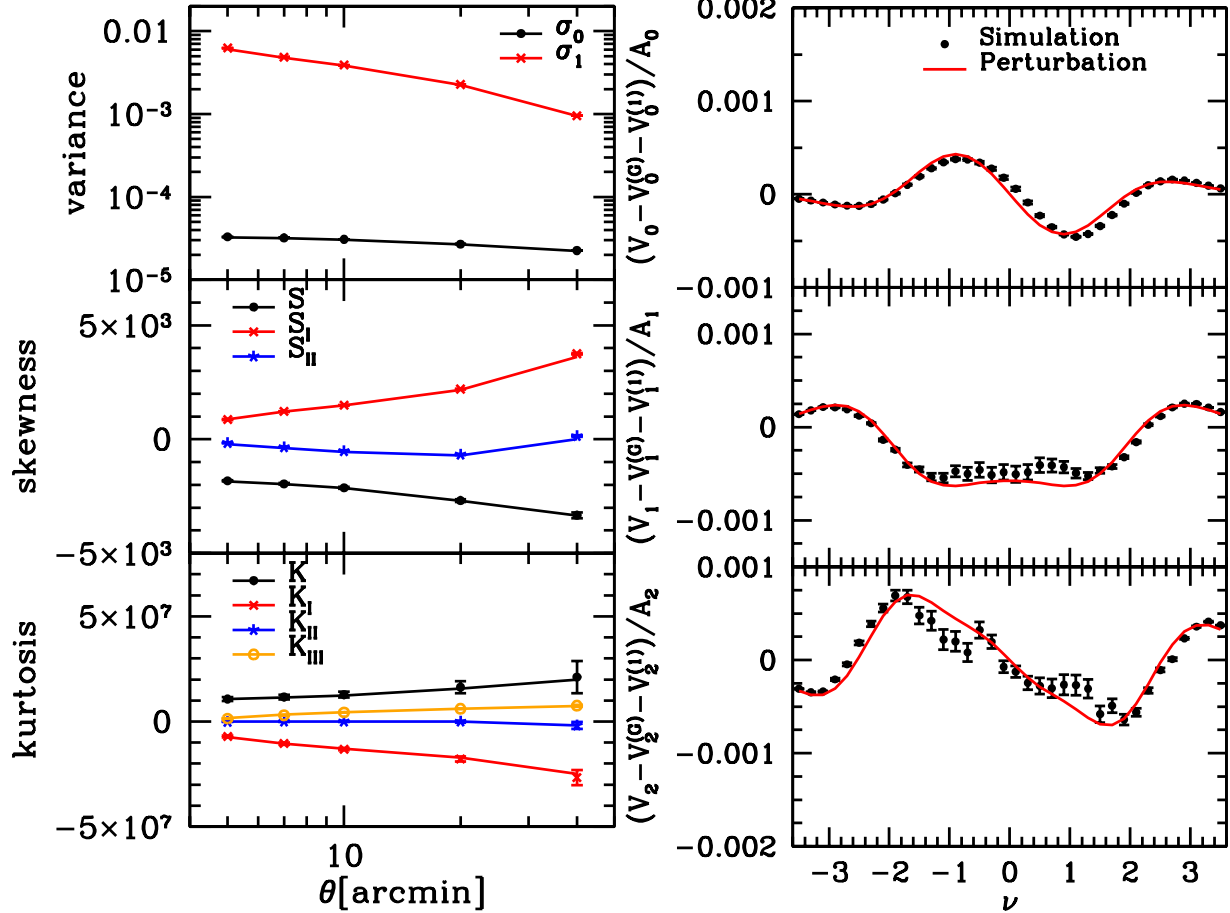
where  $p_k$  denote NG parameters such as  $f_{\text{NL}}$ ,  $\tau_{\text{NL}}$  and  $g_{\text{NL}}$  and subscript  $i$  and  $j$  of MFs denote different bins of threshold  $\nu$ , different kinds of MFs, and different smoothing scales  $\theta_s$ . We estimate the covariance matrix of MFs using 6000 realizations of Gaussian CMB maps including WMAP7 observational effects described in the previous section. For the chi-square measurement, we reduce the binning number to 18 from 36 original bins. The reduction of binning does not affect the results, which means that the binning number of 18 is enough that the result is converged. The maximum number of the side length of the covariance matrix is 270 corresponding to 18 bins of  $\nu \times$  three kinds of MFs  $\times$  five different  $\theta$ . We have checked that 6000 realizations are enough for the fitting results to be converged.

Assuming that the covariance derivative  $\partial C_{ij}/\partial p_i$  is negligible, the Fisher matrix is simply given by

$$F_{kk'} = \sum_{ij} \frac{\partial V_i}{\partial p_k} C_{ij}^{-1} \frac{\partial V_j}{\partial p_{k'}}. \quad (39)$$

We use NG CMB simulation maps and test if the above chi-square estimations generate the expected distribution of  $k$ -th NG parameter with the mean of the input value and the error expected from the Fisher matrix as  $[(F^{-1})_{kk}]^{1/2}$ . Fig.

**Figure 3.** *Left:* variance, skewness and kurtosis of NG simulations with  $f_{\text{NL}}^{(\text{loc})} = 300$  using CMB simulation maps with local-type NG (Elsner & Wandelt 2009) (symbols). The lines show the theoretical predictions based on the perturbation theory. *Right:* second-order correction of MFs in the same NG simulation maps smoothed at  $\theta = 10$  arcmin (symbols) by subtracting the Gaussian term  $V_k^{(\text{G})}$  and the first-order correction  $V_k^{(1)}$ . The NG simulations do not include the  $g_{\text{NL}}$  component and thereby the second-order correction comes from  $\tau_{\text{NL}}$  corresponding to  $36f_{\text{NL}}^{(\text{loc})2}/25 \simeq 1.296 \times 10^5$ . For comparison, perturbative predictions are written in the lines. The simulations include the WMAP beam and noise for the V+W co-added map and a pixel window function at each  $\theta$ .



5 shows the distribution of best-fit values of  $f_{\text{NL}}$ ,  $\tau_{\text{NL}}$  from full NG simulations and  $g_{\text{NL}}$  from NG simulations in Sachs-Wolfe approximation. The details of NG simulations are written in the previous subsection. Averaged values are respectively  $f_{\text{NL}} = 100 \pm 47 (-100 \pm 48)$  against the input of  $100 (-100) \pm 48$ , and  $\tau_{\text{NL}}/10^4 = 12.3 \pm 8.6 (12.4 \pm 9.1)$  against the input of  $13 \pm 8.5$ , and  $g_{\text{NL}}/10^5 = 10 \pm 1.76$  against the input of  $10 \pm 1.5$ . We find that our method well reproduces the input values of NG parameters and the error estimations using the Fisher matrix (eq.[39]) provide reasonable measurement error. The mean value of  $\tau_{\text{NL}}$  is found to be underestimated by 5%, which may be due to the incompleteness of the theoretical estimation of the kurtosis parameters. The systematic error is, however, much smaller than the statistical error of  $\tau_{\text{NL}}$  and the effect on the final result is small.

### 3.4 Comparison of constraints from MFs and skewness/kurtosis

Perturbative corrections of MFs are determined by skewness (eq:[8]) and kurtosis parameters (eq.[26]) upto 2nd order. The

parameters carry the NG information and hence their measured values can be directly used to limit the NG parameters. For consistency checks, we compare the constraints on NG parameters estimated from MFs with those estimated directly from skewness and kurtosis parameters (hereafter we call them “moments”) using WMAP mock simulation maps. Fig. 6 shows the distribution of  $f_{\text{NL}}^{(\text{loc})}$  estimated from MFs (red), and those from skewness values (blue). We find that the sample variance are comparable and thus MFs and the moments have similar power to constrain  $f_{\text{NL}}^{(\text{loc})}$ . We also plot the difference of the bestfit values of  $f_{\text{NL}}^{(\text{loc})}$  from the MFs and the skewness divided  $\sqrt{2}$ . The limits from the MFs and the moments do not completely agree because the weights on skewness parameters in MFs are not equal. The difference is smaller than the dispersion of the distribution of  $f_{\text{NL}}$ , which means that the measurements of MFs and moments are strongly correlated.

**Figure 4.** *Left:* same as Fig. 3 but for NG simulations in the Sachs-Wolfe approximation. The NG parameters are  $f_{\text{NL}}^{(\text{loc})} = 100$  and  $g_{\text{NL}} = 10^6$  in which the contribution of  $\tau_{\text{NL}}$  is negligible. *Right:* comparison of the NG correction of each MF between the perturbative theory (solid lines) and the NG simulations (filled circles). First- and second-order perturbative corrections are shown with the dotted and dashed lines, respectively.

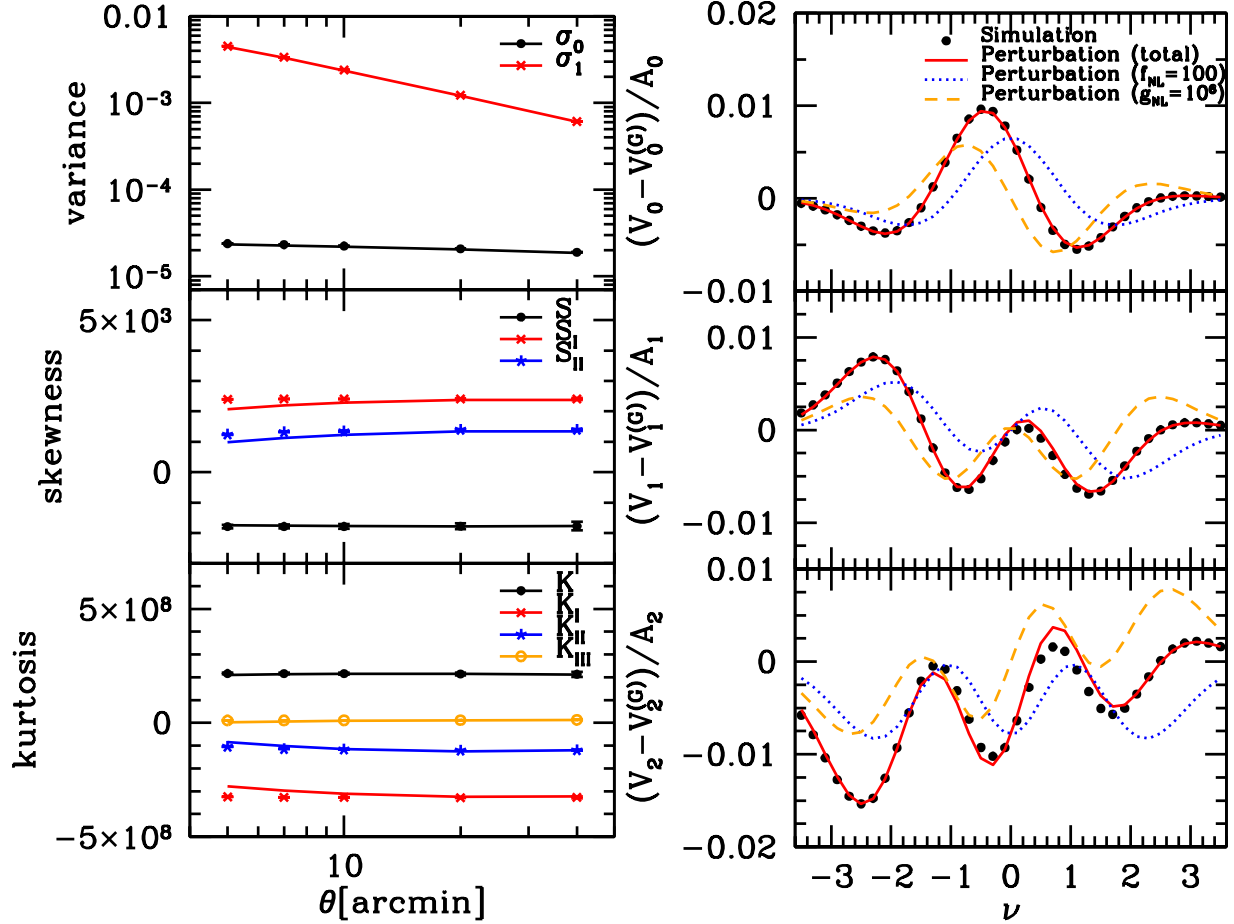


**Figure 5.** *Left:* distribution of the bestfit values of  $f_{\text{NL}}^{(\text{loc})}$  estimated from 1000 NG simulation maps in which the input values of  $f_{\text{NL}}^{(\text{loc})} = \pm 100$ ; *Middle:* distribution of  $\tau_{\text{NL}}$  estimated from 1000 NG simulation maps with the input values of  $f_{\text{NL}}^{(\text{loc})} = \pm 300$ , that is, the corresponding  $\tau_{\text{NL}} = 1.296 \times 10^5$ ; *Right:* distribution of  $g_{\text{NL}}$  estimated from 1000 NG simulations in the Sachs-Wolfe approximations. The input values of NG parameters are  $f_{\text{NL}}^{(\text{loc})} = 100$  and  $g_{\text{NL}} = 10^6$ . The lines show the Gaussian distribution with its mean of the input values and the dispersion given by the square root of the inverse of the Fisher matrix  $(F^{-1})_{kk}^{1/2}$ .

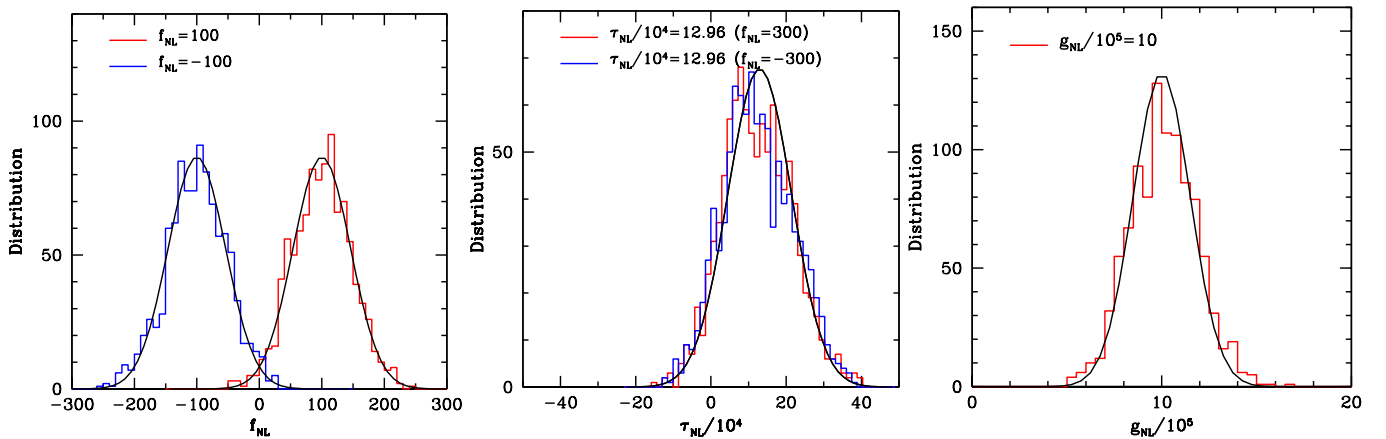
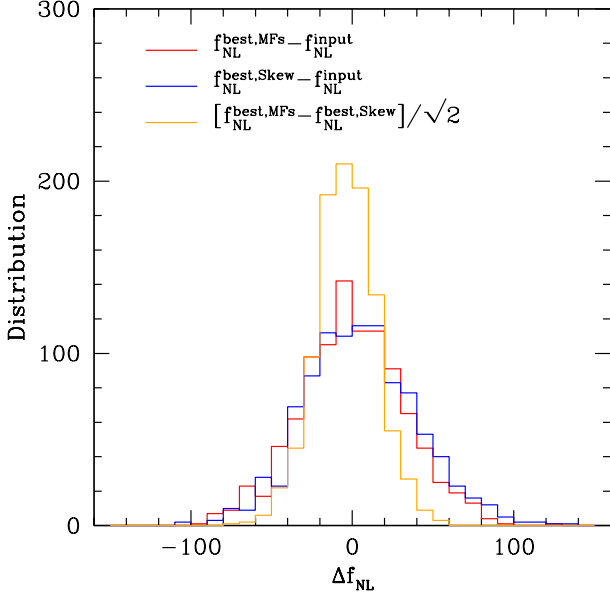


**Figure 6.** Distribution of the bestfit values of  $f_{\text{NL}}^{(\text{loc})}$  around the input value  $f_{\text{NL}}^{\text{input}} = 100$  using 1000 NG simulation maps. We obtain the bestfit values using two different measurements: MFs (red lines) and three skewness parameters (blue lines). The differences between these two measurements are also plotted with the yellow lines.

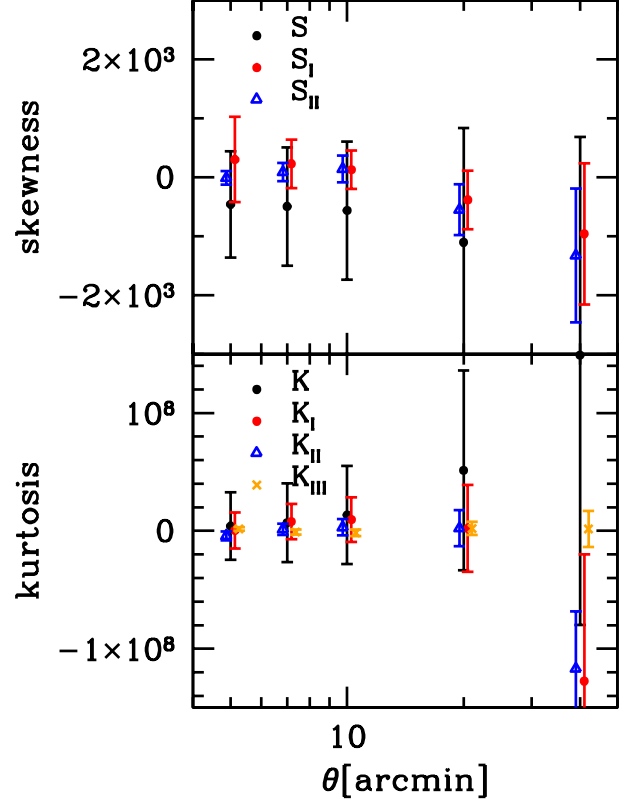


#### 4 APPLICATION TO WMAP 7-YEAR DATA

In the previous section, we show that the perturbation works even including the various observational effects. We apply the perturbative formulae to WMAP 7-year temperature maps and give limits on the NG parameters. Fig. 7 shows the MFs of WMAP 7-year V+W co-added maps at different smoothing scales. We subtract Gaussian term  $V_k^{(G)}$  from the observed MFs to focus on the deviation from Gaussian. For comparison, we plot the perturbative formulae with the bestfit values of  $f_{\text{NL}}^{(\text{loc})}$ ,  $\tau_{\text{NL}}$ , and  $g_{\text{NL}}$ . The 1st-order ( $f_{\text{NL}}^{(\text{loc})}$ ) and 2nd-order ( $\tau_{\text{NL}}$  and  $g_{\text{NL}}$ ) contributions are shown with dotted and dashed line, respectively. The differences are consistent with zero for all MFs at different smoothing scales. Fig. 8 shows the skewness and kurtosis parameters of the same WMAP data at different smoothing scales, which are also consistent with zero.

Table 2 lists the limits on  $f_{\text{NL}}$ ,  $\tau_{\text{NL}}$  and  $g_{\text{NL}}$ . The constraining power is strongest at  $\theta=10$  or 7 arcmin scales because the noise is dominated at smaller scales. Maps of different smoothing scales have different scale information and hence combining results from different  $\theta$  maps provide stronger constraint. These constraints take into account the point source effect and its contribution is marginalized over. All types of primordial NG parameters we consider are consistent with zero. The constraints from MFs are weaker than the optimal estimator based on the bispectrum (Komatsu et al. 2011) and on the trispectrum (Smidt et al. 2010). This is because that the skewness and kurtosis parameters lose configuration information on the bispectrum and the trispectrum. Again we stress that the consistency check from MFs are important to check the systematic effects. It may be interesting that the bestfit value of  $\tau_{\text{NL}}$  from MFs is slightly inclined to be negative because the negative value of  $\tau_{\text{NL}}$  is not allowed for all of multi-field inflation models by the inequality relation  $\tau_{\text{NL}} > 36/25 f_{\text{NL}}^{(\text{loc})2}$

**Figure 8.** Three skewness and four kurtosis parameters measured from WMAP 7-year data at different smoothing scales of  $\theta$ . The definitions of the skewness and kurtosis parameters are given in the equations (8) and (26), respectively.



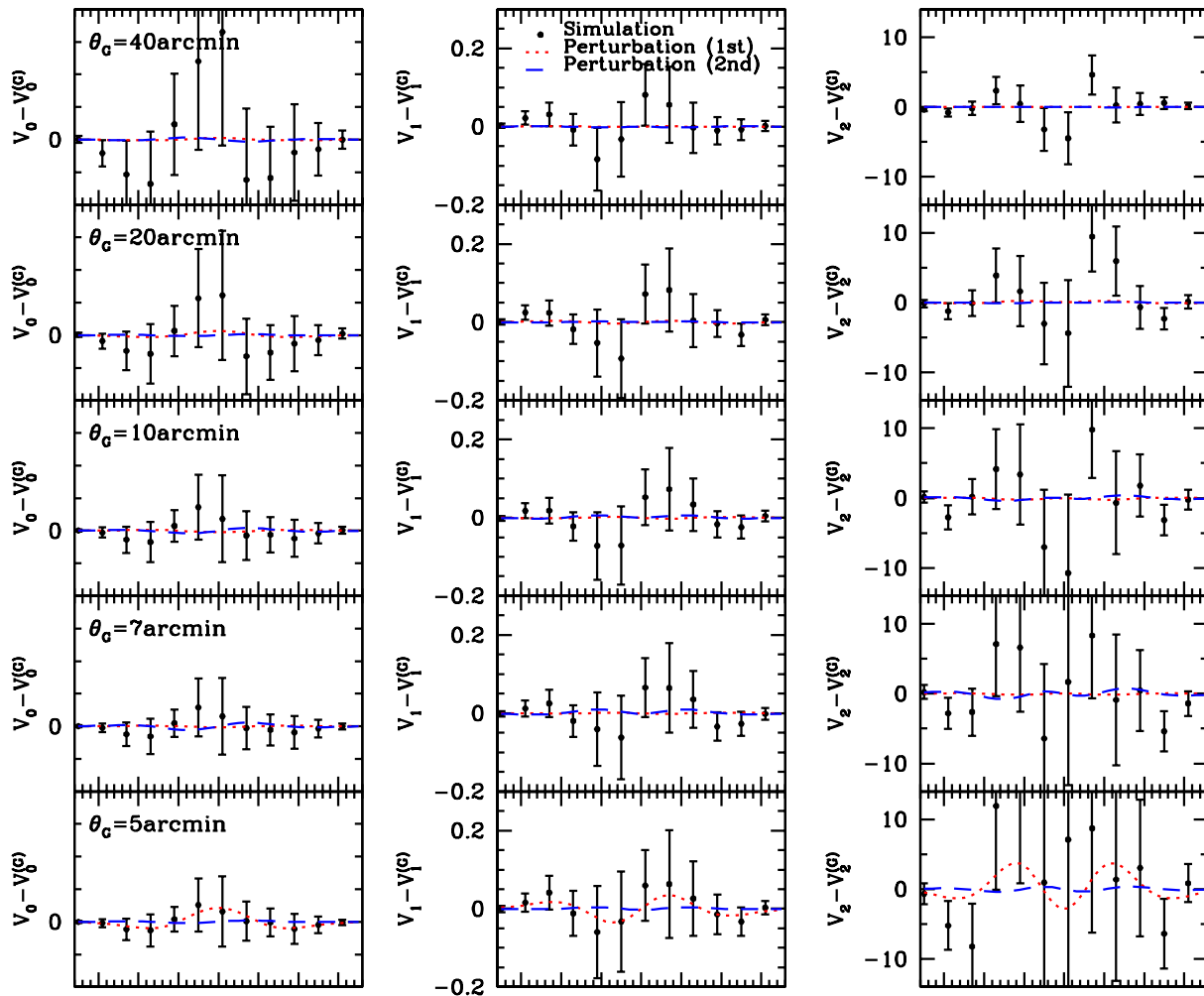
(Suyama & Yamaguchi 2008). This inclination is stronger before marginalization of point source effect as seen in Table 3, however the significance is still very small. We also give the limits from different frequency bands listed in Table 4. The differences between different frequency maps are within 1 sigma of statistical error, which means that the frequency-dependent systematics such as Galactic foreground do not affect our results so much. The results from MFs and moments (skewness and kurtosis) are also consistent and their difference is within  $1\sigma$  statistical error.

#### 5 SUMMARY AND DISCUSSIONS

We first apply the perturbative formulae of MFs including second-order NG to WMAP 7-year data and give limits on  $\tau_{\text{NL}}$  and  $g_{\text{NL}}$  as well as local-type, equilateral-type and orthogonal-type  $f_{\text{NL}}$ . Consistency check using different estimators are important to obtain more robust results because different estimators are sensitive to different aspects and systematics. We find no evidence of NG from any type of NG components and then obtain the limits on each NG parameter:  $f_{\text{NL}}^{(\text{loc})} = 20 \pm 42$ ,  $f_{\text{NL}}^{(\text{eq})} = -121 \pm 208$ , and  $f_{\text{NL}}^{(\text{ort})} = -129 \pm 171$ ,  $\tau_{\text{NL}}/10^4 = -7.6 \pm 8.7$  and  $g_{\text{NL}}/10^5 = -1.9 \pm 6.4$ . Our result is consistent with the previous works using the estimators of bispectrum and trispectrum. Constraining  $\tau_{\text{NL}}$  is important for testing multiple inflation models which must satisfy the inequality condition  $\tau_{\text{NL}} > 36/25 f_{\text{NL}}^2$ . Our limit on  $\tau_{\text{NL}}$  is con-



**Figure 7.** Three MFs for WMAP 7-year temperature maps at different  $\theta=40, 20, 10, 7,$  and  $5$  arcmin from the top to bottom. The Gaussian term  $V_k^{(G)}$  is subtracted to focus on the deviation from Gaussian. For reference, the first and second-order perturbative corrections with the bestfit values of  $f_{NL}^{(loc)}$ ,  $\tau_{NL}$  and  $g_{NL}$  are plotted, respectively.



sistent with zero, but the bestfit value of  $\tau_{NL}$  is inclined to be negative even after subtracting point source effects. Upcoming CMB experiments such as Planck will give statistically better results.

Large-scale structure offers another test to study the presence of primordial NG. Scale-dependent bias of halo clustering also provides a powerful probe of primordial NG (Dalal et al. 2008) and observational constraints  $-29 < f_{NL}^{(loc)} < 70$  (95% C.L.) are obtained (Slosar et al. 2008). Desjacques & Seljak (2010) give constraints on  $g_{NL}$  as  $-3.5 \times 10^5 < g_{NL} < 8.2 \times 10^5$  (95% C.L.) from the halo mass function and halo bias. Combining galaxy bispectra is also useful to constrain the primordial NG including the higher-order NGs  $\tau_{NL}$  and  $g_{NL}$  (Jeong & Komatsu 2009; Nishimichi et al. 2010).

The secondary effects like a coupling between the integrated Sachs-Wolfe effect and the gravitational lensing (Goldberg & Spergel 1999) may contaminate the measurement; however, the estimation is small of the order of  $f_{NL} \sim 3$  (Komatsu et al. 2011). In this paper we give limits on the three types of  $f_{NL}$ s and  $\tau_{NL}$  and  $g_{NL}$  locally given. In general, there is still a wide range of NG such as isocurvature

NG (Kawasaki et al. 2008; Hikage et al. 2009). The equilateral type of  $g_{NL}$  has been also given by Mizuno & Koyama (2010). The application to the other types of NG is a future work.

## 6 ACKNOWLEDGMENTS

We acknowledge James Fergusson for carefully reviewing the manuscript and providing very useful comments. We also thank Eiichiro Komatsu for helpful comments. This work is supported by Grant-in-Aid for Scientific Research from the Ministry of Education, Science, Sports, and Culture of Japan No. 24740160 (C. H.).

## REFERENCES

- Alishahiha, M., Silverstein, E., Tong, D., 2004, Phys. Rev. D, 70, 123505  
 Acquaviva V., Bartolo N., Matarrese S., Riotto A., 2003, Nuclear Phys. B, 667, 119

**Table 2.** Limits on NG parameters from WMAP 7-year V+W co-added maps at different smoothing scales  $\theta$  and when combined. We consider five NG parameters: quadratic NGs in local type  $f_{\text{NL}}^{(\text{loc})}$ , equilateral type  $f_{\text{NL}}^{(\text{eq})}$ , orthogonal type  $f_{\text{NL}}^{(\text{ort})}$ , and cubic NGs of  $g_{\text{NL}}$ , and  $\tau_{\text{NL}}$ . We list the constraints from MFs in the upper part and moments (i.e., three skewness and four kurtosis parameters) in the lower part of the table. The point source effect is marginalized over for all these limits.

measurement	$\theta$	$f_{\text{NL}}^{(\text{loc})}$	$f_{\text{NL}}^{(\text{eq})}$	$f_{\text{NL}}^{(\text{ort})}$	$\tau_{\text{NL}}/10^4$	$g_{\text{NL}}/10^5$
MFs	100	$-207 \pm 296$	$-2860 \pm 5540$	$260 \pm 523$	$-180 \pm 196$	$10 \pm 28$
	70	$-117 \pm 173$	$-7400 \pm 4360$	$-2 \pm 399$	$-86 \pm 105$	$0.7 \pm 18$
	40	$14 \pm 86$	$-1350 \pm 3930$	$-119 \pm 261$	$-24 \pm 41$	$3.5 \pm 11$
	20	$6 \pm 54$	$-361 \pm 2400$	$-58 \pm 204$	$-0.3 \pm 17$	$0.8 \pm 8.1$
	10	$3 \pm 53$	$-21 \pm 585$	$-25 \pm 195$	$-2.9 \pm 11$	$-1.1 \pm 7.6$
	7	$39 \pm 83$	$-354 \pm 768$	$-118 \pm 252$	$-6.2 \pm 11$	$-3.9 \pm 8.0$
	5	$82 \pm 127$	$-879 \pm 1300$	$-168 \pm 299$	$-3.0 \pm 15$	$-1.1 \pm 9.8$
	Combined	$20 \pm 42$	$-121 \pm 208$	$-129 \pm 171$	$-7.6 \pm 8.7$	$-1.9 \pm 6.4$
Moments	100	$-104 \pm 387$	$-8240 \pm 5380$	$-518 \pm 758$	$-216 \pm 205$	$15.7 \pm 44.3$
	70	$-163 \pm 204$	$-6610 \pm 4200$	$22 \pm 518$	$-83 \pm 99$	$9.9 \pm 23.4$
	40	$-55 \pm 90$	$-3840 \pm 3810$	$73 \pm 288$	$-43 \pm 37$	$2.0 \pm 11.4$
	20	$-18 \pm 55$	$715 \pm 2440$	$24 \pm 212$	$3.6 \pm 14$	$1.8 \pm 7.8$
	10	$15 \pm 54$	$-139 \pm 588$	$-77 \pm 203$	$-3.4 \pm 9.6$	$-2.1 \pm 7.1$
	7	$51 \pm 84$	$-436 \pm 770$	$-165 \pm 261$	$-4.0 \pm 9.3$	$-2.6 \pm 7.6$
	5	$84 \pm 133$	$-846 \pm 1340$	$-186 \pm 314$	$-2.2 \pm 13$	$-0.5 \pm 9.4$
	Combined	$31 \pm 40$	$-132 \pm 196$	$-145 \pm 178$	$-6.3 \pm 8.0$	$-4.1 \pm 5.8$

**Table 3.** Same as the combined limits in Table 2 but for the limits before marginalization of point source effect.

measurement	$\theta$	$f_{\text{NL}}^{(\text{loc})}$	$f_{\text{NL}}^{(\text{eq})}$	$f_{\text{NL}}^{(\text{ort})}$	$\tau_{\text{NL}}/10^4$	$g_{\text{NL}}/10^5$
MFs	Combined	$17 \pm 41$	$-129 \pm 198$	$-129 \pm 171$	$-10.5 \pm 8.1$	$-1.4 \pm 6.4$
Moments	Combined	$36 \pm 40$	$-77 \pm 188$	$-154 \pm 177$	$-4.3 \pm 7.6$	$-4.4 \pm 5.8$

- Arkani-Hamed, N., Creminelli, P., Mukohyama, S., Zaldarriaga, M., 2004, *J. Cosmol. Astropart. Phys.*, 4, 1
- Babich D., Creminelli P., Zaldarriaga M. 2004, *J. Cosmol. Astropart. Phys.*, 8, 9
- Bartolo N., Matarrese S., Riotto A., 2006, *J. Cosmol. Astropart. Phys.*, 6, 24
- Buchbinder E. I., Khoury J., Ovrut B. A., 2007, *J. High Energy Phys.*, 11, 76
- Chen X., Easther R., Lim E. A., 2007, *J. Cosmol. Astropart. Phys.*, 6, 23
- Creminelli, P., Senatore, L., 2007, *J. Cosmol. Astropart. Phys.*, 11, 10
- Creminelli P., Senatore L., Zaldarriaga M., 2007, *J. Cosmol. Astropart. Phys.*, 3, 19
- Curto A., Martínez-González E., Barreiro R. B., Hobson M. P., 2011, *MNRAS*, 417, 488
- Dalal, N., Doré, O., Huterer, D., Shirokov, A., 2008, *Phys. Rev. D*, 77, 123514
- Desjacques, V., Seljak, U., 2010, *Phys. Rev. D*, 81, 023006
- Dvali, G., Gruzinov, A., Zaldarriaga, M., 2004, *Phys. Rev. D*, 69, 083505
- Elsner, F., Wandelt, B. D., 2009, *ApJS*, 184, 264
- Falk T., Madden R., Olive K. A., Srednicki M., 1993, *Phys. Lett. B*318, 354
- Fergusson J. R., Regan D. M., Shellard E. P. S., 2010, arXiv:1012.6039
- Gangui A., Lucchin F., Matarrese S., Mollerach S., 1994, *ApJ*, 430, 447
- Gold. B. et al., 2011, *ApJS*, 192, 15
- Goldberg D. M., Spergel D.N., 1999, *Phys. Rev. D*, 59, 103002
- Gupta S., Berera A., Heavens A. F., Matarrese S., 2002, *Phys. Rev. D*, 66, 043510
- Hikage, C., Komatsu, E., Matsubara, T., 2006, *ApJ*, 653, 11
- Hikage, C., Matsubara, T., Coles, P., Liguori, M., Hansen, F. K., Matarrese, S., 2008, *MNRAS*, 389, 1439
- Hikage C., Koyama K., Matsubara T., Takahashi T., Yamaguchi M., 2009, *MNRAS*, 398, 2188
- Jeong, D., Komatsu, E., 2009, *ApJ*, 703, 1230
- Kawasaki, M., Nakayama, K., Sekiguchi, T., Suyama, T., Takahashi, F., 2008, *JCAP*, 11, 19
- Komatsu, E., Spergel, D. N., 2001, *Phys. Rev. D*, 63, 63002
- Komatsu, E. et al., 2011, *ApJS*, 192, 18
- Koyama K., Mizuno S., Vernizzi F., Wands D., 2007, *J. Cosmol. Astropart. Phys.*, 11, 24
- Kogo, N., Komatsu, E., 2006, *Phys. Rev. D*, 73, 083007
- Linde A. D., Mukhanov V., 1997, *Phys. Rev. D*, 56, R535
- Lim, E. A., Simon, D., 2012, *J. Cosmol. Astropart. Phys.*, 1, 48
- Lyth D. H., Ungarelli C., Wands D., 2003, *Phys. Rev. D*, 67, 023503
- Maldacena J. M., 2003, *J. High Energy Phys.*, 5, 13
- Matsubara, T., 2003, *ApJ*, 584, 1
- Matsubara, T., 2010, *Phys. Rev. D*, 81, 083505
- Mecke, K. R., Buchert, T., & Wagner, H. 1994, *A&A*, 288, 697
- Mizuno, S., Koyama, K., 2010, *J. Cosmol. Astropart. Phys.*, 10, 2
- Moss I., Xiong C., 2007, *J. Cosmol. Astropart. Phys.*, 4, 7

**Table 4.** Limits on the NG parameters in different frequency bands. All of the limits are obtained from MFs (Upper) or Moments (Lower) by combining different  $\theta_s$  maps and the point source effect is marginalized over.

Estimator	band	$f_{\text{NL}}^{(\text{loc})}$	$f_{\text{NL}}^{(\text{eq})}$	$f_{\text{NL}}^{(\text{ort})}$	$\tau_{\text{NL}}/10^4$	$g_{\text{NL}}/10^5$
MFs	Q+V+W	22 ± 43	-185 ± 211	-216 ± 172	-10.6 ± 8.9	-1.9 ± 6.3
	Q	21 ± 45	-5 ± 264	-94 ± 178	-7.5 ± 10.8	-4.4 ± 6.9
	V	33 ± 43	-61 ± 220	-143 ± 174	-6.5 ± 9.4	-2.7 ± 6.7
	W	12 ± 44	-102 ± 219	-98 ± 174	-7.5 ± 10.8	-4.4 ± 6.9
Moments	Q+V+W	25 ± 41	-69 ± 199	-90 ± 181	-10.4 ± 8.1	-4.8 ± 5.8
	Q	11 ± 44	-48 ± 241	-29 ± 188	-12.5 ± 9.8	-5.6 ± 6.3
	V	35 ± 41	-62 ± 206	-118 ± 180	-3.1 ± 8.7	-2.8 ± 6.1
	W	36 ± 41	-91 ± 206	-137 ± 179	-9.3 ± 8.8	-5.6 ± 6.1

- Natoli P., et al., 2010, MNRAS, 408, 1658  
 Nishimichi, T., Taruya, A., Koyama, K., Sabiu, C., J. Cosmol. Astropart. Phys., 7, 2  
 Okamoto, T., Hu, W., 2002, Phys. Rev. D, 66, 63008  
 Salopek D. S., Bond J. R., 1990, Phys. Rev. D, 42, 3936  
 Seery D., Lidsey J. D., 2005, J. Cosmol. Astropart. Phys., 6, 3  
 Schmalzing, J., & Buchert, T., 1997, ApJ, 482, L1  
 Senatore, L., Tassev, S., Zaldarriaga, M. 2009, J. Cosmol. Astropart. Phys., 8, 31  
 Slosar, A., Hirata, C., Seljak, U., Ho, S., Padmanabhan, N., 2008, J. Cosmol. Astropart. Phys., 8, 31  
 Smidt, J., Amblard, A., Byrnes, C. T., Cooray, A., Heavens, A., Munshi, D., 2010, Phys. Rev. D, 81, 123007  
 Suyama, T., Takahashi, T., Yamaguchi, M., Yokoyama, S., 2010, J. Cosmol. Astropart. Phys., 12, 30  
 Suyama, T., Yamaguchi, M., 2008, Phys. Rev. D, 77, 023505  
 Vielva, P., Sanz, J. L., 2010, MNRAS, 404, 895  
 Yadav, A. P. S., Wandelt, B., D., 2008, Phys. Rev. Lett., 100, 181301